Reliability Assessment of Actuator Architectures for Unmanned Aircraft ⋆

Raghu Venkataraman, [†,‡] **Márk Lukátsi,** [*] **Bálint Vanek,** [*] **and Peter Seiler** [†]

[*] *Institute for Computer Science and Control, Hungarian Academy of Sciences (MTA SZTAKI)*
[†] *Department of Aerospace Engineering and Mechanics, University of Minnesota (UMN AEM)*
[‡] *corresponding author, (e-mail: venka085@umn.edu)*

Abstract: A reliability assessment framework is presented for small unmanned aerial vehicles. The analysis considers several candidate architectures with different numbers of controllable surfaces and servos. It is assumed that a servo fault detection algorithm is available and affected by known rates of false alarms and missed detections. The aircraft flight envelope is analyzed to determine the fault levels for which the aircraft can still be flown at a trim point. For these "flyable" fault levels, it is assumed that the flight control law can be reconfigured to safely land the aircraft. Finally, the probability of catastrophic failure is estimated based on the histogram of (pre-fault) control command distributions, mean time between failure of the individual servos, and missed detection and false alarm rates. In applying the framework to assess the reliability of the candidate architectures, several interesting observations on design trade-offs are made.

1. INTRODUCTION

The unmanned aerial vehicle/system (UAV/UAS) industry is undergoing rapid transformation due to the emergence of several commercial applications. The commercial UAV market is projected to surpass the military market in the coming years, primarily driven by new technological capabilities, lower production costs, and new regulatory framework [Frost & Sullivan, 2011]. Despite the positive forecast, there are regulatory and technical challenges. On the regulatory side, US and EU aviation authorities are developing long-term frameworks for integrating UAVs into the national airspace [European Commission, 2014]. In February 2015, the US Federal Aviation Administration [2015] released a Notice of Proposed Rulemaking that specifies UAV operational limitations. On the technical side, challenges such as sense & avoid, communication, and human factors need to be addressed.

The reliability of most existing UAVs are far below those of manned commercial and military aircraft. The MQ-1 Predator recorded an accident rate of 13.7 for every 100,000 hours for its first 10 years of operation. The MQ-9 Reaper has fared better than the Predator, with 3.17 mishaps per 100,000 hours. This is partly due to its triple redundant flight control system and the more rigorous systems engineering approach behind it [Whitlock, 2014]. Hardware redundancy should be used judiciously on UAVs because of associated size, weight, and power costs [Spitzer, 2001]. Most commercial UAVs fly with single-string components and use only two control surfaces [Rester et al., 2013]. As compared to redundant hardware, cross-functional control surfaces can provide an efficient way of increasing the reliability.

⋆ The research leading to these results has received funding from the European Union Seventh Framework Programme (FP7/2007- 2013) under grant agreement no. FP7-AAT-2012-314544.
This work was supported by the National Science Foundation under Grant No. NSF/CNS-1329390 entitled "CPS: Breakthrough: Collaborative Research: Managing Uncertainty in the Design of Safety-Critical Aviation Systems".

This paper makes contributions in the area of UAV reliability assessment. Specifically, this paper presents a framework that may be applied to assess the reliability of UAV actuator architectures. Actuator architecture refers to the placement of actuators and control surfaces. The framework is applied to several candidate actuator architectures. These architectures and the assumptions in the framework are explained in section 2. In addition to being used as a reliability analysis tool, the framework can help understand the design trade-offs inherent in systems engineering. One of the trade-offs that is explored is between reliability and number of redundant components.

Traditional aircraft reliability methods model the effects of the fault as a binary process: a fault, if present, will lead to a catastrophic failure. This research introduces a probabilistic notion to faults. In doing so, some credit is given to the fact that some failure modes can be tolerated (with sub-par performance), but do not necessarily lead to catastrophic failure.

2. PROBLEM FORMULATION

The aircraft system reliability is quantified via the probability of catastrophic failure. Catastrophic failure occurs when the UAV cannot reach a proper landing site. Actuator failure is one of the major causes of catastrophic failure. Specifically, actuators contain a lot of moving parts and are amongst the least reliable components. (Engine failure is not considered because it is assumed that the aircraft can glide to a safe landing.) There are several actuator failure modes such as stuck, runaway, loss of efficiency, oscillatory [Goupil, 2010], etc. The last three failure modes are more common in large aircraft where large loads are present. This paper only considers stuck actuator faults, with runaway faults being a special case. After an actuator fails, a path will be generated to a landing site. The generated path will consist of some basic flight paths such as straight & level, turning, and descending flight. These requirements can be translated into a minimal flight envelope in the flight path angle - heading rate plane (see section 4).

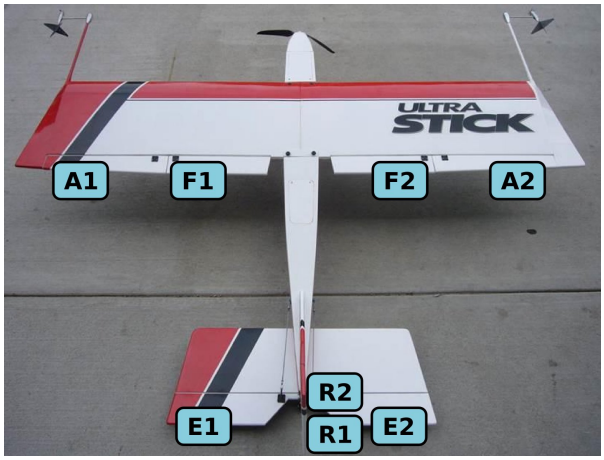

Fig. 1. The BALDR UAV with the control surfaces labeled (A – aileron, F – flap, E – elevator, R – rudder).

Table 1. Actuator architectures.

Conf.	Ailerons	Elevators	Rudders	Flaps
v0(4)	Coupled	Coupled	Coupled	Coupled
v1(4)	Decoupled	Coupled	Coupled	None
v2(4)	Coupled	Decoupled	Coupled	None
v3(3)	Coupled	Coupled	Coupled	None
v4(3)	Decoupled	Coupled	None	None

The framework is applied on a small UAV called BALDR, which is based on the Ultra Stick 120 airframe. A simulation environment is available for this UAV. The centerpiece of the environment is the high-fidelity, nonlinear, six degrees-of-freedom aircraft model. The aerodynamic parameters were estimated based on wind tunnel tests [Owens et al., 2006, Hoe et al., 2012]. The entire simulation environment, hardware details, and flight data have been made open-source and can be freely downloaded from the University of Minnesota [2014].

The BALDR UAV has eight unique aerodynamic control surfaces (see figure 1): split elevators $(E1, E2)$, split rudders $(R1, R2)$, ailerons $(A1, A2)$, and flaps $(F1, F2)$. Each of the eight surfaces is actuated by an independent servo motor. Different combinations of the eight surfaces allow for different actuator architectures to be defined. The sign convention of the control surfaces is as follows. A trailing edge down deflection of the elevators, ailerons, and flaps is considered positive. A trailing edge left deflection of the rudders is considered positive. In addition, all the surfaces have a deflection range of $[-25°, +25°]$. Increasing the number of servos on an aircraft increases reliability, but it also adds to the cost and weight. To analyze this trade-off, five actuator architectures are defined in table 1. The number of servos is given in parenthesis in the first column.

The configurations v0 to v4 were chosen because they are representative of the most common actuator architectures found in small UAVs. As an example, consider the presence/absence of flaps across the five configurations. Flaps are not very common in small UAVs since they perform a very specific function and are not used for the majority of the flight duration. Since flaps are atypical, four configurations (v1 to v4) are not equipped with flaps. The only configuration that is equipped with flaps is v0. This is because v0 is only used for flight envelope assessment in section 4. On the other hand, all configurations have elevators and ailerons since these are required control surfaces. The eight different control surfaces of the

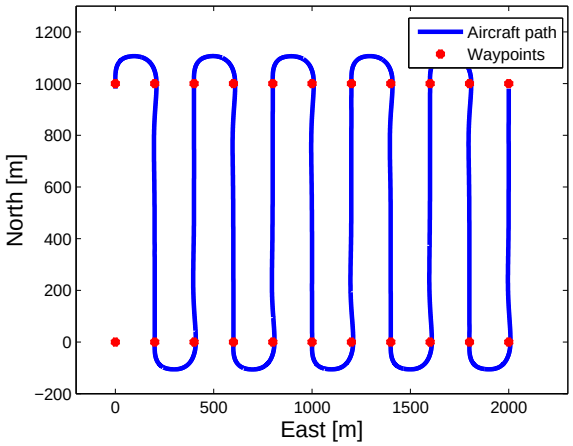

Fig. 2. Aircraft path during area scanning mission.

BALDR are coupled differently depending on the actuator configuration. As an example, for the v0 configuration, $A1 = -A2$, $E1 = E2$, $R1 = R2$, and $F1 = F2$.

The five configurations cover different combinations of pitch & roll control authorities. For example, elevators, when decoupled, contribute to both pitching and rolling. The configurations are representative of small UAV architectures because they were chosen by balancing the need to maximize the pitch and roll control authorities against the need to minimize the number of servos. For example, an architecture that has decoupled elevators and decoupled ailerons is not considered. This is because, while such an architecture will exhibit higher reliability than any other, it would also require the use of many servos. In choosing the five configurations, it was ensured that the number of servos was at most equal to four. It should be noted that the BALDR UAV has many more control surfaces than will be found on a typical small UAV.

Several assumptions are made to make the analysis tractable. First, it is assumed that a fault detection and isolation (FDI) algorithm is used to detect actuator faults. The FDI algorithm could either be built-in tests (self-diagnostics within actuators) or centralized monitoring systems. For simplicity, only statistical properties, such as missed detection and false alarm rates, are considered. Second, it is assumed that if the aircraft is trimmable after a fault has occurred, an appropriate reconfigurable control law is available. In other words, transitions between trim points are without loss of control. Finally, it is assumed that multiple faults occur with negligible probabilities.

The analysis method has three distinct steps: (1) determining the control surface distributions, (2) determining the stuck surface ranges, and (3) estimating the probability of catastrophic failure. The probability distributions of the surface deflections are used to compute the probabilities of the surfaces being stuck in ranges where faults cannot be tolerated. The ranges for each surface are computed through flight envelope assessment. Finally, the probability of catastrophic failure is estimated.

3. DISTRIBUTION OF CONTROL SURFACES

The first step in the analysis is determining the distribution of the aircraft's control surfaces. The distributions are influenced by several factors such as: mission profile, control law, exogenous disturbances (sensor noise, wind gusts, & turbulence), etc. Control laws significantly affect

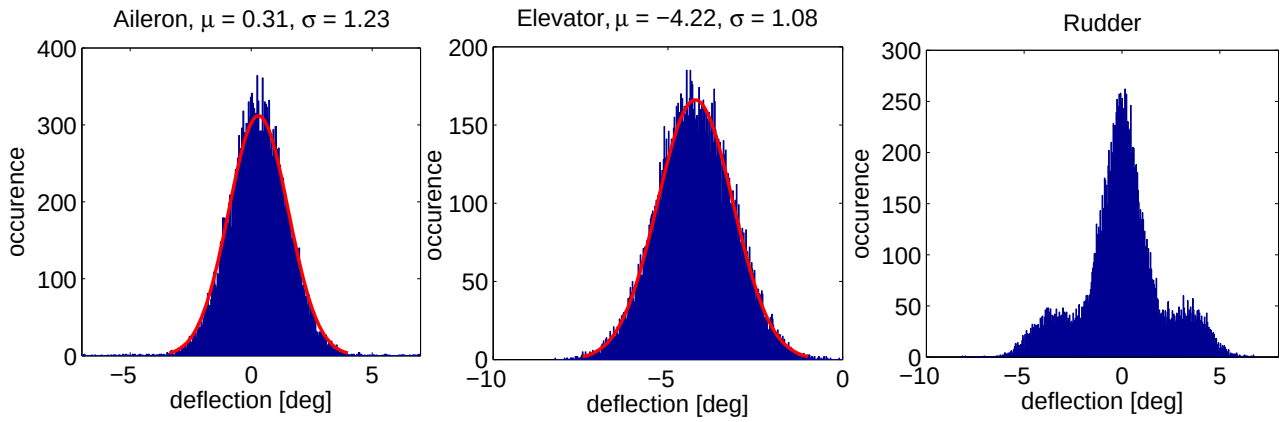

Fig. 3. Control surface distributions for straight & level flight. Number of bins is 400. Simulation time is 588s.

the distributions and, thereby, the overall reliability. As an example, the rudder will have different distributions depending on whether the control law is tuned for coordinated turns or yaw rate damping. More generally, the gains of the control law affect the shape of the distributions. The shape of the distributions, in turn, affect the overall reliability. By properly tuning the control law, the shape of the distributions can be tailored to meet performance as well as reliability requirements.

Histograms of control surface deflections can be plotted from flight data or simulations. Subsequently, probability density functions can be estimated. Flight data may not always be available for arbitrary mission profiles. A more analytical approach would break down a mission into modes of straight & level, turning, ascending, and descending flights. If the control surface distributions are known for these modes, the overall distributions can be constructed by combining them with appropriate weights.

$$p_i(\delta) = \sum_{j=1}^{n} p_i(\delta|mode = j)p(mode = j) \tag{1}$$

where $p_i(\delta|mode = j)$ is the probability density function (PDF) of the ith control surface in mode j and $p(mode = j)$ is the probability of mode j. In this analytical approach, only a small library of PDFs need to be stored in order to be able to generate PDFs for arbitrary missions.

Figure 2 shows a typical area scanning path for BALDR. It consists of three modes: straight & level, left, and right banked flights. Figure 3 shows the histograms of the control surfaces for the straight & level mode. Similar distributions are obtained for the left and right banked turns, but are not shown here. Normal distributions are fitted to ailerons and elevators as they are approximately Gaussian. On the other hand, rudder distributions appear to be multi-modal. The histograms only depend on the mission being executed and not on the actuator architecture. Before a fault occurs, all actuator architectures are controlled by the same baseline control law. This baseline control law actuates all surfaces as if they were coupled. In other words, the baseline control law is designed for architecture v0. It is only after a fault occurs that the actuator architecture matters.

The probability of being in each mode is estimated from the mission profile as the fraction of time spent in that mode. For mission in figure 2, the probabilities of the modes can be calculated from the geometry of the flight path. The waypoints are 1000m and 200m apart in the North and East directions, respectively. The resulting probabilities are 0.13 for both left and right turns and 0.74 for straight flight.

4. FLIGHT ENVELOPE ASSESSMENT

This section gives a cursory introduction to aircraft flight envelopes, since this concept is important for the subsequent section. The aircraft equations of motion [Nelson, 1998] can be described in the nonlinear state-space form as shown in equations 2 and 3.

$$\dot{x} = f(x, u) \tag{2}$$

$$y = h(x, u) \tag{3}$$

In these equations, $x \in \mathbb{R}^n$ is the state vector, $u \in \mathbb{R}^m$ is the input vector, and $y \in \mathbb{R}^p$ is the output vector. In addition, $f : \mathbb{R}^n \times \mathbb{R}^m \to \mathbb{R}^n$ is the state function and $h : \mathbb{R}^n \times \mathbb{R}^m \to \mathbb{R}^p$ is the output function. The state vector is: $x = [\phi, \theta, \psi, p, q, r, u, v, w]^T$. Here, ϕ, θ, and ψ are the Euler angles of the aircraft. The aircraft's angular velocity in the body-fixed frame are: roll rate (p), pitch rate (q), and yaw rate (r). The airspeed components in the body-fixed frame are u, v, and w. We also define a reduced order state vector that does not contain ψ: $x_r = [\phi, \theta, p, q, r, u, v, w]^T$. x_r is used in the definitions of the flight envelopes.

For configuration v0, there are only four unique aerodynamic inputs. In addition, the throttle is τ. Consequently, the input vector is $u = [\tau, E, R, A, F]$. As expected, the input vector will change depending on the actuator configuration. The studies conducted in this paper make use of certain elements in the output vector (y). The airspeed, angle of attack, and angle of sideslip are denoted by V, α, and β, respectively. The flight path climb angle and heading rate are denoted by γ and $\dot{\psi}$, respectively.

Aircraft typically fly around equilibrium or trim points. These are operating points at which some state derivatives are zero, and others have constant values. The collection of all such trim points defines the steady flight envelope ($\mathbb{F}$) of the aircraft, as shown in equation 4.

$$\mathbb{F} = \{(\bar{x}, \bar{u}) : \dot{\bar{x}}_r = 0, \dot{\bar{u}} = 0\} \tag{4}$$

A subset of the flight envelope is straight & level flight. This subset is mathematically described in equation 5. The key property of this subset is the zero flight path angle.

$$\mathbb{F}_{straight,level} = \{(\bar{x}, \bar{u}) : f(\bar{x}, \bar{u}) = 0, \bar{p} = \bar{q} = \bar{r} = 0, \bar{\gamma} = 0, \dot{\bar{u}} = 0\} \tag{5}$$

When the aircraft descends steadily, at a constant negative flight path angle, the envelope is described by equation 6.

$$\mathbb{F}_{steady,descent} = \{(\bar{x},\bar{u}) : f(\bar{x},\bar{u}) = 0,\ \bar{p} = \bar{q} = \bar{r} = 0,$$
$$\bar{\gamma} < 0,\ \dot{\bar{u}} = 0\} \quad (6)$$

Steady banked turns at constant altitude are defined by constant heading rate. For example, $\dot{\psi} < 0$ describes left banked turns, as shown in equation 7.

$$\mathbb{F}_{banked,left} = \{(\bar{x},\bar{u}) : \dot{\bar{x}}_r = 0,\ \dot{\psi} < 0,\ \bar{\gamma} = 0,\ \dot{\bar{u}} = 0\} \quad (7)$$

These subsets can be computed by applying numerical optimization techniques to the nonlinear aircraft model that was introduced in section 2. The model can be trimmed and linearized, using routines developed in-house, at any operating point within the flight envelope. For straight & level flight, operating points are best expressed as pairs of (V, α). A rectangular grid of such (V, α) pairs is generated for $V \in [10, 40]\mathrm{m\,s^{-1}}$ and $\alpha \in [0°, 20°]$. The grid resolution is $0.1\mathrm{m\,s^{-1}}$ and $0.1°$. The nominal flight condition for BALDR is $(V, \alpha) = (23\mathrm{m\,s^{-1}}, 4.72°)$. The trim routine is called at each grid point after being initialized with the nominal flight condition. For a specific subset, the trim routine finds the minimum of a nonlinear, multi-variable cost function subject to the appropriate constraint (equations 5 – 7). Matlab's Optimization Toolbox contains the *fmincon* function that is well suited for this purpose. This optimization problem is non-convex and, in general, has multiple local minima. The *fmincon* function returns the minimum that is closest to the initial condition. [Freeman and Balas, 2014] conducted a similar trim state discovery for another Ultra Stick 120 version. The work presented in this paper draws on the results therein and connects them to the probability of catastrophic failure in section 5. A more thorough treatment of aircraft flight envelopes can be found in [Wilborn and Foster, 2004].

A limited flight envelope assessment is presented only for configuration v0. The envelope corresponding to longitudinal straight & level flight can be used to determine the stuck ranges for the elevator and flaps. This envelope is shown in the $V \times \alpha$ plane in figure 4 and in the $F \times E$ plane in figure 5. Trim points are marked by colored crosses in both these figures. In figure 4, the trim points are colored based on the value of the flap deflection. There are several interesting observations. First, as expected, there is an inverse relationship between V and α. Second, since a nonlinear aircraft model is being trimmed, the inputs and outputs are implicitly constrained. As a result, the flight envelope has well-defined boundaries, as seen in figure 4.

The high speed boundary defines the highest achievable airspeeds and lowest achievable angles of attack. Conversely, at the stall boundary, the stall angle of attack (15°) is reached at low airspeeds. The high speed and stall boundaries are due to output constraints. The other two boundaries are due to input saturation. The TE down/up flap boundary defines trim points for which flaps are deflected to ±25° (trailing edge down/up). It is interesting to note that within these boundaries, fixed flap deflections define isolines that follow the general shape of the envelope. Although this envelope is plotted for configuration v0, certain isolines define the envelopes for other configurations. As an example, consider configuration v3, where no flaps are used. The flight envelope for this configuration would simply be the green isoline for $F = 0$ shown in figure 4.

In figure 5, the trim points are colored based on the value of α. Three important conclusions can be drawn from this figure. Firstly, it is seen that trim points exist for the entire range of flap deflections, as shown by the TE up/down flap boundaries. Secondly, there are no trim points for

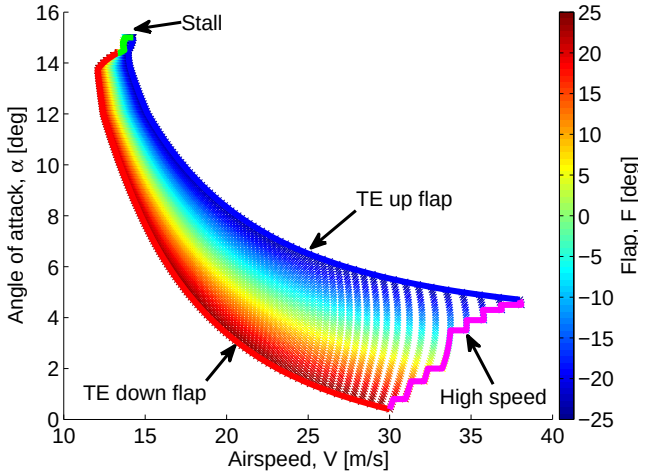

Fig. 4. Longitudinal flight envelope in the $V \times \alpha$ plane.

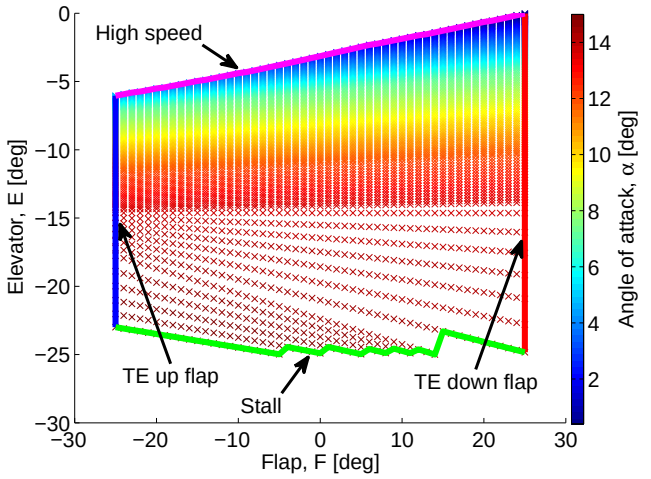

Fig. 5. Longitudinal flight envelope in the $F \times E$ plane.

a positively deflected elevator. This implies that if the elevator was to get stuck positively, the result would be catastrophic. As an example, for configuration v3 ($F = 0$), trim points exist for the elevator range $[-25°, -4°]$. It is seen that, for any given flap deflection, the high speed boundary is reached when the elevator is deflected to its highest trimmable value. Conversely, the stall boundary is reached for the lowest trimmable value of the elevator.

A stuck surface fault is called *allowable* if the aircraft can safely fly home in the presence of this fault. In order to safely fly home, the aircraft should be able to execute some limited maneuvers. The aircraft should be able to fly straight & level, execute either left or right banked turns with some minimum $\dot{\psi}$, and descend steadily at some minimum γ. These limited maneuvers form the minimal flight envelope in the $\gamma \times \dot{\psi}$ plane (figure 6). It is reasoned that as long as the actual flight envelope, in the presence of a stuck fault, is larger than this minimal flight envelope, the aircraft can safely fly home.

For this research, the maximum required turning radius is 87m. This is sufficiently larger than the minimum achievable turning radius of 54m, while still allowing for reasonably large heading rates. At a nominal airspeed of $V = 20\mathrm{m\,s^{-1}}$, an 87m turning radius corresponds to a heading rate of $\pm 13°/s$. The minimum required flight path angle is chosen as $\gamma = -3°$ since this is

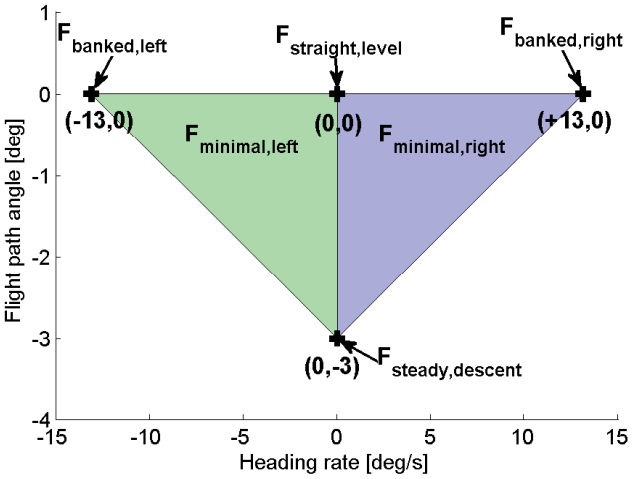

Fig. 6. Minimal flight envelope

Table 2. Allowable stuck surface ranges

Config.	Elevator(s)	Rudder(s)	Aileron(s)
v1	[-25,-1]	[-25,+25]	[-25,+25]
v2	[-25,+25]	[-25,+25]	[-11,+12]
v3	[-25,-4]	[-25,+25]	[-7,+10]
v4	[-25,-1]	N/A	[-25,+25]

representative of typical glide slopes. The four points shown in figure 6 define two triangles: $\mathbb{F}_{minimal,left}$ and $\mathbb{F}_{minimal,right}$. Furthermore, it is assumed that if trim points exist at the vertices of either of these two triangles, trim points exist in all of the corresponding triangle.

For any given stuck fault, in order to safely fly home, at least one trim point needs to be found in each of the subsets $\mathbb{F}_{straight,level}$ and $\mathbb{F}_{steady,descent}$, and either of the subsets $\mathbb{F}_{banked,left}$ and $\mathbb{F}_{banked,right}$. In other words, a stuck fault is called allowable if trim points can be found either in $\mathbb{F}_{minimal,left}$ or $\mathbb{F}_{minimal,right}$. In checking for the existence of trim points, no explicit constraints (such as a zero sideslip angle requirement) are placed on V, α, and β.

The following steps describe the calculation of the allowable stuck surface ranges. First, the trimmable range for each surface is calculated at each of the four points shown in figure 6. Then, the intersection of these trimmable ranges is calculated between $\mathbb{F}_{straight,level}$, $\mathbb{F}_{steady,descent}$, and $\mathbb{F}_{banked,left}$. This intersection is called the trimmable range for $\mathbb{F}_{minimal,left}$. In a similar way, $\mathbb{F}_{minimal,right}$ is calculated. The union of $\mathbb{F}_{minimal,left}$ and $\mathbb{F}_{minimal,right}$ is defined as the allowable stuck surface range.

The allowable stuck surface ranges for v1,...,v4 are given in Table 4. For configurations that have a single elevator (v1, v3, v4), it is seen that the range is never positive, i.e. no trim points exist for positively stuck elevator. However, the allowable range is $[-25°, +25°]$ when split elevators are present (v2). Another interesting observation is that stuck rudder faults can always be tolerated as long as no explicit constraints are placed on β. Lastly, decoupled ailerons (v1 and v4) have the full allowable range as compared to coupled ailerons (v2 and v3). The allowable stuck surface ranges presented here in conjunction with the distribution of control signals, presented in section 3, allow for the computation of the probability of catastrophic failure for each of the four configurations. It is generally observed that cross-functionality in the aerodynamic control surfaces helps increase the overall reliability of the UAV.

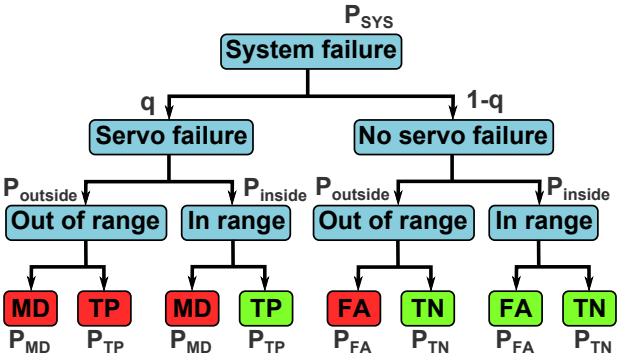

Fig. 7. Fault tree (MD – missed detection, TP – true positive, FA – false alarm, TN – true negative).

5. PROBABILITY OF CATASTROPHIC FAILURE

The final step of the analysis is computing the probability of catastrophic failure (P_{SYS}). Figure 7 shows a fault tree. The first level of the tree is the servo failure rate (q), which is the inverse of the mean time between failures (MTBF). The next level captures the positional probabilities of the control surfaces. The final level captures false alarm (P_{FA}) and missed detection (P_{MD}) rates. Events that lead to catastrophic failure are marked red and the others green. The probability of the ith surface being outside its allowable range is $P_{out,i} = 1 - \int_l^u p_i(\delta_i) d\delta_i$. The probability of the ith surface getting stuck outside the allowable range is $qP_{out,i}$. The total probability of catastrophic failure is:

$$P_{SYS} = \sum_{i=1}^{N} qP_{out,i} + qP_{in,i}P_{MD} + (1-q)P_{out,i}P_{FA} \quad (8)$$

Missed detections lead to catastrophic failure, irrespective of the surface position. False alarms lead to catastrophic failure, but only outside the allowable range. It is assumed that faults inside the range can be tolerated.

The framework is applied to configurations v1, ..., v4. Figure 8 shows the probabilities as a function of servo MTBF with $P_{MD} = 0.05$ and $P_{FA} = 0.01$. The servo MTBF range from common R/C-grade [Murtha, 2009] to high performance [Office of the Secretary of Defense, 2003]. For example, Volz Servos GmbH [2009] servos have a high MTBF (1000 hours). Typical built-in tests cover more than 95% of faults [Boeing Aerospace Company, 1987]. Hence, $P_{MD} = 0.05$ in figure 8. It is assumed that current FDI algorithms allow for $P_{FA} = 0.01$.

From figure 8, the probability of failure for v3 is two orders of magnitude greater than that of the other architectures. This is because configuration v3 has no decoupled surfaces implying there is very little cross-functionality. v1 is the second-to-worst architecture, despite having 4 servos. Compared to v3, v1 has an extra servo that decouples the ailerons and extends their allowable range to $[-25°, +25°]$. This greatly increases the reliability of v1 relative to v3. However, v1 (4 servos) is less reliable than v4 (3 servos). This demonstrates that increasing the number of servos does not necessarily increase the reliability.

Finally, the two most reliable configurations are v2 (4 servos) and v4 (3 servos). For low servo MTBF, the probability of failure is lower for v4. On the other hand, for high servo MTBF, the probability of failure is lower for v2. Excluding the rudder, both v2 and v4 use a three-servo architecture. While v2 has coupled ailerons and decoupled elevators, v4 has decoupled ailerons and coupled elevators. The presence/absence of the rudder in v2 and

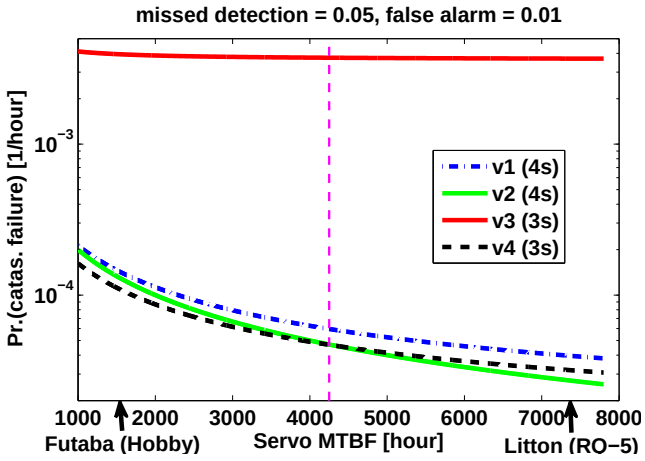

Fig. 8. Prob. of failure as a function of servo MTBF.

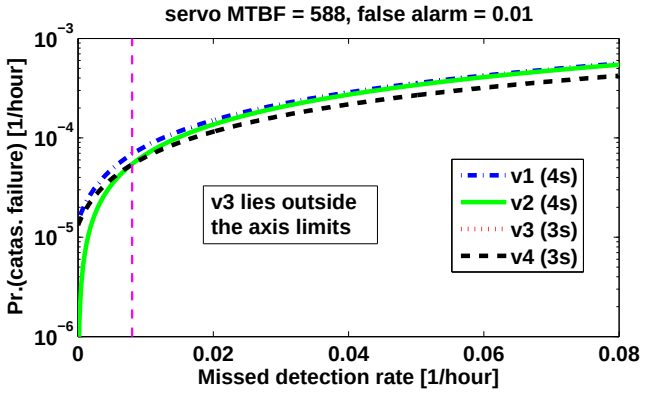

Fig. 9. Prob. of failure as a function of missed detection.

v4 is the reason for the total number of servos being different. However, table 4 indicates that rudder faults of any magnitude can be tolerated. Thus, the difference between v2 and v4 is primarily driven by the architecture of the elevators and ailerons. It is generally concluded that when low reliability servos are used, an architecture that decouples the ailerons (v4) is more reliable. On the other hand, when high reliability servos are used, an architecture that decouples the elevators (v2) is more reliable.

It would be naive to generalize this conclusion any further. The plots shown in figure 8 are functions of several variables such as: servo reliability, actuator placement, surface coupling, mission, etc. In general, there is a complex interplay between these different variables as shown by Rice and McCorkle [1979]. All the candidate architectures considered in this case study are single-string designs. Thus, the cross-functionality of the surfaces is a major contributor to the overall reliability of the UAVs. Increasing the cross-functionality between surfaces can help increase the overall reliability with minimal increases in size and weight. Traditional reliability analyses do not take credit for the cross-functionality between components. By considering the flight envelope of the UAV, the framework presented is able to take credit for the cross-functionality between surfaces. In addition to the flight envelope assessment, modeling the stochastic nature of surface faults and connecting them to the mission profile ultimately enables this framework to yield less conservative estimates of the overall reliability of the candidate actuator architectures.

Figure 9 shows variation with missed detection rate for fixed MTBF and P_{FA}. As before, v3 is the least reliable and lies above the other curves. A trade-off that is similar to the one observed with servo MTBF is seen. For low missed detection rates, decoupled elevators (v2) is more reliable. For high missed detection rates, decoupled ailerons (v4) is more reliable.

6. CONCLUSION

A reliability assessment framework is presented in this paper for unmanned aircraft actuator architectures. The framework treats control surface faults probabilistically. In addition, cross-functionality between surfaces is explicitly treated using flight dynamics. In applying the framework to five candidate actuator architectures, several interesting and non-intuitive observations are made. Not all of these observations have simple explanations. It is reasoned that the proposed framework might be useful to unmanned aircraft designers, while considering reliability in the design process. The non-intuitive observations are in themselves justifications for applying more rigorous assessment methods, than relying on mere rules of thumb.

REFERENCES

Boeing Aerospace Company. Built-in-test verification techniques, 1987.

European Commission. A new era for aviation opening the aviation market to the civil use of remotely piloted aircraft systems in a safe and sustainable manner, 2014.

Federal Aviation Administration. Notice of proposed rulemaking, February 2015.

P. Freeman and G. Balas. Actuation failure modes and effects analysis for a small uav. In *American Control Conference*, 2014.

Frost & Sullivan. Study analysing the current activities in the field of uav. *EC Enterprise and Industry*, 2011.

P. Goupil. Oscillatory failure case detection in the A380 electrical flight control system by analytical redundancy. *Control Engineering Practice*, 18(9):1110 – 1119, 2010.

G. Hoe, D. Owens, and C. Denham. Forced oscillation wind tunnel testing for faser flight research aircraft. In *AIAA AFM Conference*, 2012.

J. F. Murtha. An evidence theoretic approach to design of reliable low-cost uavs. Master's thesis, Virginia Polytechnic Institute and State University, 2009.

R. C. Nelson. *Flight Stability and Automatic Control*. McGraw-Hill, 1998.

Office of the Secretary of Defense. Unmanned aerial vehicle reliability study, 2003.

D. Owens, D. E. Cox, and E. A. Morelli. Development of a low-cost sub-scale aircraft for flight research: The faser project. In *25th AIAA Aerodynamic Measurement Technology and Ground Testing Conference*, 2006.

M. Rester, P. Spruyt, T. De Groeve, O. Van Damme, and A. Ali. Unmanned aerial systems for rapid mapping. Technical report, JRC Scientific & Policy Reports, 2013.

J. W. Rice and R. D. McCorkle. Digital flight control reliability - effects of redundancy level, architecture, and redundancy management technique. In *AIAA GNC Conference*, 1979.

C. R. Spitzer. *The Avionics Handbook*. CRC Press, 2001.

University of Minnesota. Uav research group. `www.uav.aem.umn.edu`, 2014.

Volz Servos GmbH. Endurance test da 22-30-4128, 2009.

C. Whitlock. When drones fall from the sky. *The Washington Post*, 2014.

J. E. Wilborn and J. V. Foster. Defining commercial transport loss-of-control: A quantitative approach. In *AIAA AFM Conference*, 2004.